



CrossMark
 click for updates

Cite this: *RSC Adv.*, 2015, 5, 67227

Probing the differential methane decomposition behaviors of *n*-Ni/SiO₂, *n*-Fe/SiO₂ and *n*-Co/SiO₂ catalysts prepared by co-precipitation cum modified Stöber method

U. P. M. Ashik and W. M. A. Wan Daud*

n-Ni/SiO₂, *n*-Fe/SiO₂ and *n*-Co/SiO₂ nano-catalysts were prepared by co-precipitation cum modified Stöber method and applied for thermocatalytic decomposition of methane in order to investigate their thermal stability and activity to produce greenhouse gas free hydrogen and nano-carbon. The mean particles sizes of the produced nano-catalysts obtained from BET analysis are 32.19 nm, 30.26 nm and 49.92 nm, respectively. Temperature programmed methane decomposition were conducted as a preliminary catalytic examination and further isothermal analyses were performed at 700 °C, 600 °C and 500 °C. Production of hydrogen at each experimental temperatures and corresponding carbon yield were measured. Among the three catalysts inspected, *n*-Ni/SiO₂ was found to be the most efficient one for thermocatalytic methane decomposition. Furthermore, significant catalytic stability was observed with *n*-Ni/SiO₂ at 500 °C and 600 °C. While, the rapid deactivation of the *n*-Fe/SiO₂ and *n*-Co/SiO₂ catalysts are attributed to particle agglomeration and the irregular formation of nano-carbon due to metal fragmentation. Physical and chemical characteristics of the produced nano-catalysts were investigated by N₂ adsorption–desorption measurement (BET), X-ray diffraction (XRD), transmission electron microscopy (TEM) and hydrogen-temperature programmed reduction (H₂-TPR). Produced nano-carbon were inspected with TEM, FESEM and XRD.

Received 10th June 2015
 Accepted 30th July 2015

DOI: 10.1039/c5ra10997c

www.rsc.org/advances

Introduction

Forthcoming advancements in catalysis are very reliant on the fabrication of catalytic materials with advanced features. Nowadays, investigations on catalyst technology are predominantly focusing on development of smaller materials with efficient properties like activity, selectivity and stability. The novel advancements in nanotechnology have simplified the production of very fine nano-particles with narrow size distributions less than 100 nm.¹ Hence, nano-materials can be defined as those materials having one or more dimension in the nano-meter scale (<100 nm) range. These nano-materials have gained predominant consideration because of the immense changes that occur in their physical and chemical properties when micro particles transform to nanoparticles. The catalytic performance of nano-materials is associated with their morphology, size distribution, and electronic properties. It is well known that the preparation methods, stabilizer, as well as supports selected, can individually influence all of these characteristic properties.² So far, enormous research efforts have been devoted in order to

explore the catalytic application of transition metals with size in the nano-range. Achieving nano-size is quite challenging and hence there are many techniques were developed. Those methods can be broadly classified as (i) condensation from vapor, (ii) synthesis by chemical reaction, and (iii) solid-state processes such as milling. Co-precipitation, a chemical reaction synthesis was adopted in our study to prepare adequate metal oxide nano-particles. The inherent surface characteristics of such nano-particles are highly desirable for catalysis purposes. While, those naked nanoparticles are undergoing easy aggregation at higher temperature results in its faster degradation and hence excluded from higher temperature catalytic applications.³ We have targeted to safeguard active metal phase with stable, inert and porous material by modified Stöber method.³ Henceforth, it can effectively prevent higher temperature agglomeration and tolerating its higher temperature utilizations.

The produced porous and high temperature withstanding catalysts were used for thermocatalytic decomposition of methane (TCD) to produce hydrogen and nano-carbon, two cherished products in the field of environmentally benign energy and nanotechnology. Hence, there have been intense research efforts on methane decomposition in recent years as hydrogen is a relevant raw material in chemical and petroleum

Department of Chemical Engineering, University of Malaya, 50603, Kuala Lumpur, Malaysia. E-mail: upmashik@gmail.com; ashri@um.edu.my; Fax: +60 379675319; Tel: +60 105023818; +919496844805

industries. However, a higher temperature ($>1200\text{ }^{\circ}\text{C}$) is necessary in methane decomposition process to achieve a rational yield. Hence, a variety of metal catalysts have been studied for methane decomposition with the purpose of reducing the decomposition temperature as well as the increasing conversion rate. Among them, Ni, Fe and Co based catalyst gained major attention because of their advantages like availability, low cost, better activity and stability.^{4–8} According to Takenaka *et al.*,^{9,10} Ni-based catalyst are very active in a temperature range of $400\text{ }^{\circ}\text{C}$ – $600\text{ }^{\circ}\text{C}$ for methane decomposition. And they found that Ni-based catalysts deactivated immediately at temperatures above $600\text{ }^{\circ}\text{C}$. Whereas, Fe-based catalyst are found active at higher temperature as the activation temperature of the Fe-based catalysts is much higher than that of the Ni-based catalysts.^{11–13} Furthermore, iron-based catalysts are comparatively inexpensive and non-toxic. However, it was reported that Fe-based catalysts are not active below $650\text{ }^{\circ}\text{C}$.¹⁴ It is observed that iron-based catalysts produce thin-wall nanotubes, which are the most valuable product among carbon nano-fibers.¹⁵ Cobalt is adjacent to nickel and iron in periodic system and it is found proficient for methane coupling reactions.^{16,17} The intention of this work is to implement similar preparation methodology for the preparation of Ni, Fe and Co-based catalyst and study the differences in their activity, accordingly. It was reported that nickel particles larger than 100 nm is incompetent to produce carbon nano filaments in methane decomposition because the produced carbon isolates metal from reaction medium rapidly.¹⁵ Hence, a support for the active phase is necessary in order to prevent its sintering in hydrocarbon media. However, a wide variety of dissimilar support materials were investigated to control the catalyst particle size and dispersion by physical interactions (porous support) or chemical interaction (charge transfer effect).¹⁸ Takenaka *et al.*⁹ explored influence of different catalytic supports like MgO , Al_2O_3 , SiO_2 , TiO_2 , ZrO_2 , $\text{MgO}\cdot\text{SiO}_2$, $\text{Al}_2\text{O}_3\cdot\text{SiO}_2$, $\text{H}^+\text{-ZSM-5}$, *etc.* and concluded that SiO_2 as the most efficient catalyst support for TCD to produce hydrogen and nano-carbon. Hence, we have selected SiO_2 as the support material for conserving active metal phase. The porous silica support efficaciously provide enough porosity for accessing reactant molecule to the active metal oxide.¹⁹ However, in this paper we have investigated characteristic properties of $n\text{-Ni/SiO}_2$, $n\text{-Fe/SiO}_2$ and $n\text{-Co/SiO}_2$ nano-catalysts and their activity and stability for thermal decomposition of methane. We have given equal importance to catalyst preparation and characterization, methane decomposition and characterization of produced carbon. Various techniques were adopted for physical and chemical characterization of produced nano-catalysts as follows; N_2 adsorption-desorption measurement (BET), X-ray diffraction (XRD), transmission electron microscopy (TEM) and hydrogen-temperature programmed reduction ($\text{H}_2\text{-TPR}$). Furthermore, activity and stability of catalysts were analyzed in a fixed bed pilot plant. In addition, the characterization of the formed nano-carbon fibers and tubes at various temperatures are explained with the help of TEM, FESEM and XRD.

Experimental section

Co-precipitation method was adopted for preparing fine nano-sized metal hydroxide precipitate and those hydroxides was effectively supported with silicate. Initially, nano-sized M–OH containing suspension was prepared by treating metal nitrate with ammonia solution at room temperature. Hence, agglomeration of metal oxides at comparatively higher temperature was effectively eluded. The SiO_2 support was fabricated through modified Stöber method.³ It involves the hydrolysis of a mixture of tetraethyl orthosilicate (TEOS) and octadecyl trimethoxy silane (C18TMS) with aqueous solution of ammonia in the suspension of nano-M–OH.

Chemicals used

All chemicals purchased were used without performing any further purification. Nickel(II) nitrate hexahydrate ($\text{Ni}(\text{NO}_3)_2\cdot 6\text{H}_2\text{O}$), cobalt(II) nitrate hexahydrate ($\text{Co}(\text{NO}_3)_2\cdot 6\text{H}_2\text{O}$) and octadecyl trimethoxy silane (C18TMS) were obtained from Acros Organics. Aldrich supplied iron(III) nitrate nonahydrate ($\text{Fe}(\text{NO}_3)_3\cdot 9\text{H}_2\text{O}$) and tetraethyl orthosilicate (TEOS). Ammonia solution and ethanol from R&M solutions and 99.999% hydrogen, 99.995% methane and 99.99% nitrogen were purchased from Linde Malaysia Sdn. Bhd.

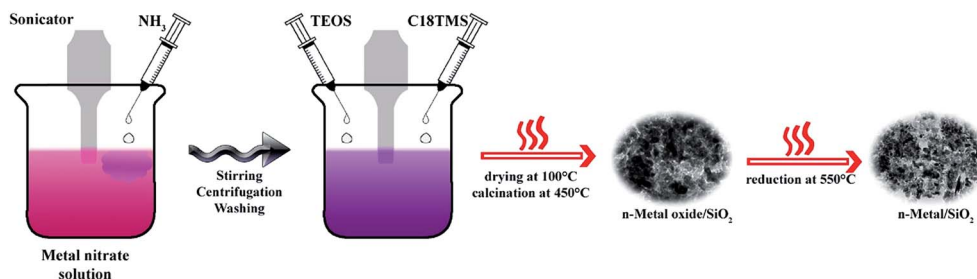
Preparation of nano-metal/ SiO_2 catalyst

0.02 mol of metal nitrate was homogeneously dissolved in 200 mL water by sonication. Dissolved metal nitrate was allowed to precipitate as corresponding hydroxide by the drop-wise addition of 6 mL of 30% NH_3 solution under sonication for 1 h . The resulting suspension was stirred for another 1 h with magnet at room temperature. Then, centrifuge the solution at 4000 RPM for 30 minutes and wash the precipitate two times with deionized water and one time with ethanol. Afterwards, the product was dispersed in 100 mL of ethanol and continuously stir for 15 h with magnet. Sonicate the suspension for 10 minutes and add 4 mL of 8 M NH_3 solution. Add 0.4 mL of TEOS and 0.4 mL C18TMS simultaneously to the basic dispersion under sonication in order to form silicate support to guard active metal phase, named modified Stöber method. The resulting mixture further sonicate for 60 minutes at room temperature. Stir the solution for further 5 hours over a magnetic stirrer. Subsequently, M–OH/ SiO_2 precipitate was separated by centrifugation and dry in an oven at $100\text{ }^{\circ}\text{C}$ for 15 hours . Separated precipitate was then converted to metal oxide/ SiO_2 by calcination at $450\text{ }^{\circ}\text{C}$ for 3 hours . Calcinated samples are named as $n\text{-NiO/SiO}_2$, $n\text{-FeO/SiO}_2$ and $n\text{-CoO/SiO}_2$. Finally, metal oxide/ SiO_2 nanocatalysts were reduced to metal/ SiO_2 by treating with 30% H_2 for 2.5 h and the reduced samples are named as $n\text{-Ni/SiO}_2$, $n\text{-Fe/SiO}_2$ and $n\text{-Co/SiO}_2$.

Schematic illustration of catalyst preparation is shown in Scheme 1.

Characterization techniques

Investigation of physicochemical properties of the catalyst done by means of different characterization methods such as N_2



Scheme 1 Schematic illustration of the fabrication of silicate supported nano-metallic catalyst.

adsorption–desorption measurement, X-ray diffraction (XRD), transmission electron microscopy (TEM), field emission scanning electron microscopy (FESEM) and hydrogen temperature programmed reduction (H_2 -TPR).

Nitrogen adsorption–desorption measurements (BET method) were carried out in Micromeritics ASAP 2020 BET apparatus at $-196\text{ }^\circ\text{C}$. Surface area, pore size distribution and structure, pore volume and the mean particle size were measured. Samples were previously degassed at $180\text{ }^\circ\text{C}$ for 4 h. The surface area was determined according to the standard Brunauer–Emmett–Teller (BET) method in a relative pressure range of 0.04–0.2 and the total volume was evaluated from the amount of adsorbed N_2 at a relative pressure (P/P_0) of about 0.98. The pore diameter distributions were calculated based on desorption isotherms by the Barrett–Joyner–Halenda (BJH) method.

PANalytical diffractometer was used to collect X-ray diffraction (XRD) patterns of the fresh and spent catalysts. Crystal phase and structure of the nano-catalysts were determined. X'pert HighScore software were used for diffractogram evaluation. Diffraction patterns of the samples were recorded with a Rigaku Miniflex with $Cu\ K\alpha$ radiation with a generator voltage and a current of 45 kV and 40 mA, respectively. The average crystallite size was obtained using the global Scherrer equation as follows:

$$D_{\text{avg}} = \frac{0.9\lambda}{\beta \cos \theta} \left(\frac{180}{\pi} \right)$$

In equation, the average crystallite size, peak length, line broadening full width at half-maxima after subtracting the instrumental line broadening (in radians), and the Bragg's angle are expressed as D_{avg} (nm), λ (1.54056 \AA), β , and 2θ , respectively. 0.9 is the Scherrer constant.

Transmission electron microscopy (TEM) images of fresh catalyst and produced nano-carbon were acquired by using FEI Tecnai™ controlled at an accelerating voltage of 200 keV. Field emission scanning electron microscopic (FESEM) images of produced nano-carbon and elemental composition of the catalysts were obtained with FEG Quanta 450, EDX-OXFORD.

Temperature-programmed reduction (H_2 -TPR) measurements were carried out using a Micromeritics TPR 2720 analyzer. Typically, 0.03 g of catalyst sample was placed in a U-tube holder and the sample was first cleaned at $130\text{ }^\circ\text{C}$ for 60

minutes by flushing with helium gas. Upon degassing, the reductive gas mixture consisting of 5% hydrogen balanced with nitrogen at a flow rate of 20 mL min^{-1} streamed through the sample. The sample was heated from $200\text{ }^\circ\text{C}$ to $700\text{ }^\circ\text{C}$ to obtain the TPR profiles of the sample.

Catalytic activity

Experimental setup. Schematic representation of catalytic methane decomposition unit is shown in Fig. 1. The fixed catalyst bed reactor constructed with stainless steel (SS310S) has the following dimension: outer diameter = 6.03 cm, wall thickness = 0.87 cm and height = 120 cm. A quartz tube (3.56 cm internal diameter, 4 cm outer diameter, and 120 cm height), obtained from Technical Glass Products (Painesville, USA), was placed inside the reactor in order to avoid interaction of feed gas with stainless steel. A quartz frit with 150 μm to 200 μm porosity was used as the catalyst bed. Temperature was supplied with a vertically mounted, three-zone tube furnace (model TVS 12/600, Carbolite, UK).

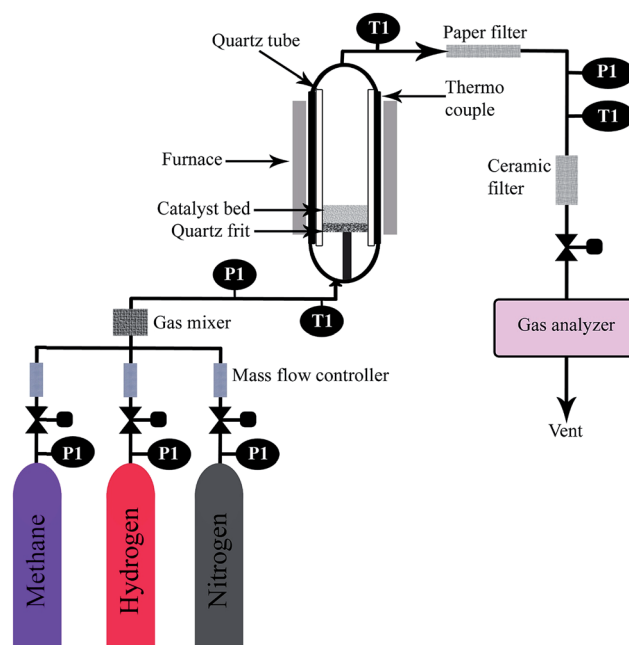


Fig. 1 Simplified schematic visualization of methane decomposition unit.

Temperature measurements were recorded by using two K-type thermocouples (1/16 in diameter, Omega, USA). The first thermocouple was fixed on the exterior surface of the stainless steel tube. The second thermocouple was inserted into the quartz tube momentarily for calibration and removed afterward from the quartz tube prior to testing because its internal copper material could affect the TCD of methane.²⁰ In addition, pressure and temperature indicators were placed at different locations to control the operating conditions. A two-differential pressure transducer (0" H₂O to 4" H₂O) was supplied by Sensicon to measure the pressure drop across the reactor. Mass flow controllers (Dwyer, USA) in the range of 0–2 L min⁻¹ were used to control the gas flow rates. The outflow gas was then cooled down to room temperature by means of an air cooler. Solid particles that had sizes greater than 2 nm and high molecular weight components were separated using two filters (38 M membrane, Avenger, USA). A calibrated Rosemount Analytical X-STREAM (UK) was used as an online analyzer to compute the mole percentage of methane and hydrogen.

Temperature programmed methane decomposition

1 g of catalyst was homogeneously distributed over catalyst bed and purge nitrogen for 30 minutes at room temperature to clean the furnace and catalyst at flow of 1 L min⁻¹. Increase the bed temperature to 550 °C with a ramp of 20 °C min⁻¹ and pass 30% H₂ in N₂ feed for 2.5 hours to reduce the metal oxide catalyst to its metallic form. Then, decrease the furnace temperature to 200 °C by air cooler under N₂ flow. Pass 99.995% methane with a flow rate of 0.64 L min⁻¹ for temperature programmed decomposition from 200 °C to 900 °C with ramp of 5 °C min⁻¹.

Isothermal methane decomposition

Catalyst bed was uniformly covered with 0.5 g of catalyst. Pure nitrogen was passed for 30 minutes in order to clean the furnace and catalyst at flow rate of 1 L min⁻¹. Then, system temperature was increased to 550 °C with a ramp of 20 °C min⁻¹. Reduction of catalyst was conducted at 550 °C by passing 30% H₂ in N₂ feed for 2.5 hours. Then, increase/decrease the temperature to reaction temperature under N₂ flow, accordingly. Once destination temperature reached, N₂ flow was replaced with 99.995% methane with a flow rate of 0.64 L min⁻¹ for evaluating methane conversion.

Results and discussion

Catalyst preparation

Nano-sized Ni, Fe and Co metal oxides were prepared by coprecipitation method using 30% NH₃ solution as a precipitating agent. Silicate support was developed by treating the metal hydroxide suspension with mixture of C18TMS and TEOS in an alcoholic medium named modified Stöber method. Hence, the alcoholic medium reduces the agglomeration of particle as well as free silicates.^{21,22} While, we haven't used any surfactants in order to prevent agglomeration of metal oxide particles. The comprehensive catalyst preparation process contains three stages as follows: (a) metal hydroxide

precipitation from the respective metal nitrate solution with 30% NH₃ solution; (b) direct silicate support formation over produced nano metal hydroxide with a mixture of C18TMS and TEOS.²³ C18TMS was added to the reaction mixture in the sense of increasing the porosity of SiO₂ support. And (c) higher temperature treatments in order to enhance its porosity. The high temperature treatments such as calcination (at 450 °C under air) and reduction (at 550 °C under 30% H₂ balanced with N₂) prior to activity examination supposed to remove all organic moieties and convert metal oxides to their metallic form. The added C18TMS helps to sparse silica polymerization and produces more pores inside the silica network after calcination. The efficient silicate support excellently prevent the particle agglomeration during those high temperature treatment. A series of characterization were conducted to enlighten the characteristics of produced nanostructures. Furthermore, activity and stability were studied for TCD at various temperature in a fixed bed pilot plant.

Characterization

The crystalline structure, size and phase purity of *n*-Ni/SiO₂, *n*-Fe/SiO₂ and *n*-Co/SiO₂ were determined by X-ray diffraction (XRD). The patterns of all those three catalysts before and after reduction at 550 °C for 2.5 hours in 30% H₂/N₂ are presented in Fig. 2(a–c). Hence, the apparent crystallite structure of catalyst has noteworthy impacts on its longevity and activity. The crystalline size corresponds to each peak calculated from the full width at half maximum of diffraction peak using Scherrer equation is provided near to peaks, those are clearly close to the mean particle size obtained from nitrogen adsorption-desorption analysis (furnished in Table 1). The strong diffraction peaks in the XRD patterns of the catalysts characterize the high crystallinity of the metallic catalysts. *n*-Ni/SiO₂ sample exhibits three major diffraction peaks corresponding to (111), (200) and (220) reflections of the solid. The diffraction peaks of *n*-NiO/SiO₂ are positioned at $2\theta = 37.2294^\circ$, 43.2752° , 62.8456° , 75.3690° and 79.3668° with *d*-spacing values 2.415 Å, 2.090 Å, 1.477 Å, 1.260 Å and 1.206 Å, respectively. All those peaks are in good agreement with standard card of cubic NiO with JCPDS no. 01-073-1523. The peaks of XRD pattern for the *n*-Ni/SiO₂ are at 44.4667° , 51.8934° and 76.3347° with *d*-spacing values 2.037 Å, 1.762 Å and 1.247 Å, respectively. Positions of these diffraction peaks are in good agreement with those are given in JCPDS no. 01-070-1849 for nickel phase. However, it also shows NiO peaks with lower intensity, indicating its incomplete reduction at mentioned condition. It is believe that the reduction with 30% hydrogen for 2.5 hours at 550 °C was adequate to convert naked *n*-NiO to *n*-Ni, while the reinforced *n*-NiO with SiO₂ needs more severe conditions for complete reduction. Hence, *n*-Ni/SiO₂ structures exhibit both metallic and metal oxide phases (Fig. 2(a)).²⁴ While, the intensity of *n*-NiO phases are found abridged after reduction process. The remaining *n*-NiO phases in the sample even after reduction diligently interact with porous silicate support, which supposed to establish a better catalysis environment results a more stable reaction course during the TCD process. However, the incomplete reduction of

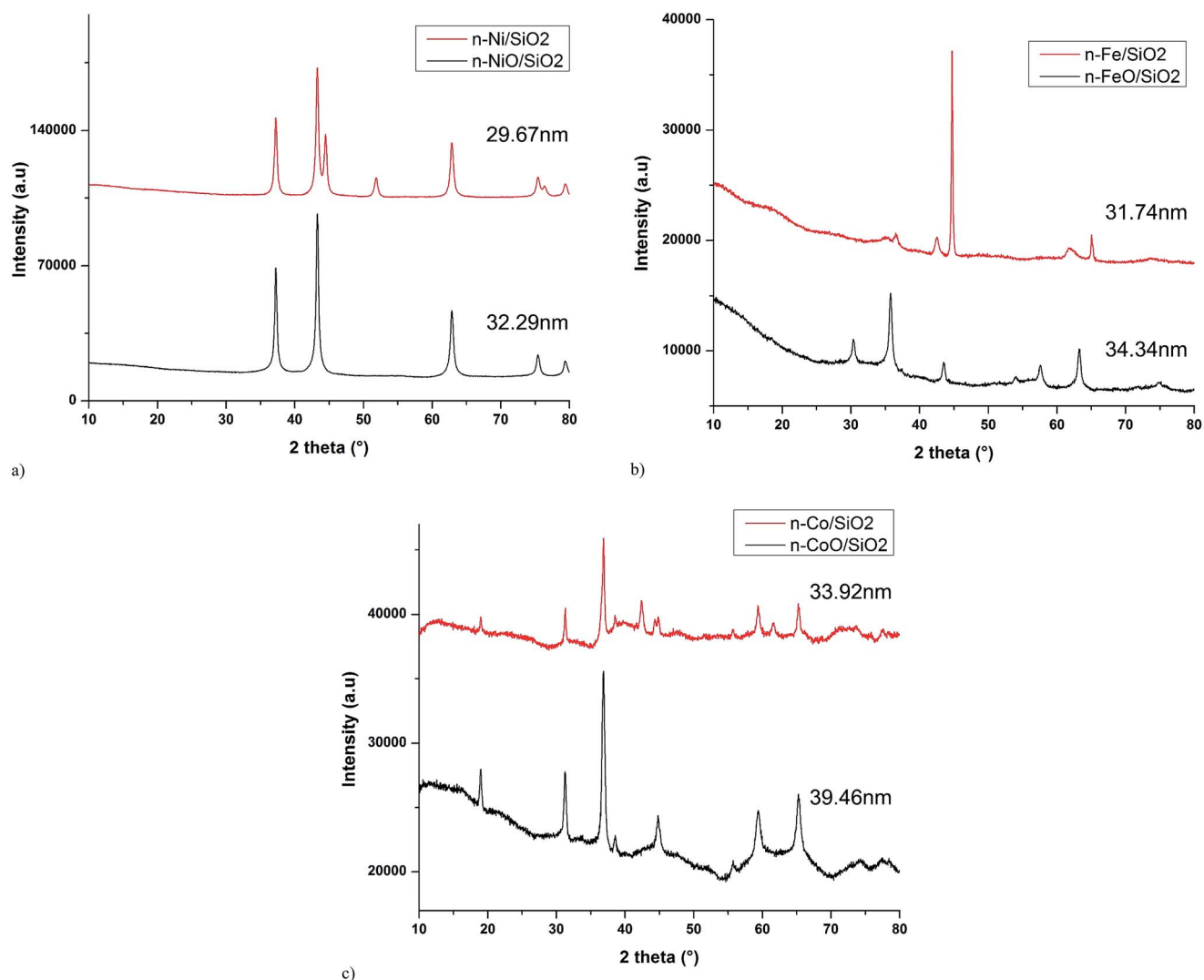


Fig. 2 XRD patterns of (a) *n*-NiO/SiO₂ and *n*-Ni/SiO₂, (b) *n*-FeO/SiO₂ and *n*-Fe/SiO₂ and (c) *n*-CoO/SiO₂ and *n*-Co/SiO₂. Average crystal sizes computed by using Scherrer equation are provided.

n-NiO phases are not retarding activity of *n*-Ni/SiO₂ during TCD process as methane itself is acting as an excellent reducing agent and hence there is no *n*-NiO phases were detected in XRD patterns after TCD (Fig. 9(a)). The absence of SiO₂ in the XRD pattern can be noticed, it is because of its X-ray amorphous characteristics and hence it was not detected in XRD. In Fig. 2(b), *n*-FeO/SiO₂, exhibits peaks centered at 2θ values as follows: 18.4802°, 30.3579°, 35.7862°, 37.3971°, 43.5235°, 53.9752°, 57.5678°, 63.3233°, 71.6516° and 74.7656°. These diffraction peaks are very closely similar to that of maghemite-Q Fe₂O₃ with JCPDS no. 00-013-0458. While, most of the FeO peaks were disappeared after reduction treatment and exhibit following peaks at 44.6929° and at 65.0464° with *d*-spacing values 2.027 Å and 1.433 Å which corresponds to iron with JCPDS no. 01-089-7194. In addition, it shows peaks for non-reduced FeO at 35.1381°, 36.5943°, 42.5573° and 61.7748° with lower intensity. *n*-CoO/SiO₂ exhibit peaks at following 2θ values: 18.9856°, 31.3425°, 36.8190°, 38.6456°, 44.8147°,

55.7140°, 59.3773°, 65.2070°, 74.2270° and 77.2868° as shown in Fig. 2(c). These peaks are showing similarity with CoO with JCPDS no. 01-074-1657. One can see that the intensity of all CoO peaks verily reduced after reduction stage.

The porous nature of the prepared *n*-NiO/SiO₂, *n*-FeO/SiO₂ and *n*-CoO/SiO₂ were explored with N₂ adsorption-desorption measurements. The corresponding N₂ adsorption-desorption isotherms and pore size distributions are presented in Fig. 3(a-c), respectively. The pore diameter distributions of the samples considered from desorption division of the isotherm were calculated using Barrett-Joyner-Halenda (BJH) method. The single point surface area, Brunauer-Emmett-Teller (BET) surface area, pore volume, average pore size and average particle size of all investigated nano-catalysts are shown in Table 1. Comparatively lower particle size and higher surface area and porosity were observed. Those catalytic activity promoting features could be attributed to the presence of silicate support. However, the silicate support is supposed to

Table 1 Physical characteristics of *n*-NiO/SiO₂, *n*-FeO/SiO₂ and *n*-CoO/SiO₂ from N₂ adsorption-desorption analysis

Catalyst	Single point SA ^a (m ² g ⁻¹)	BET SA (m ² g ⁻¹)	Micropore area ^b (m ² g ⁻¹)	Micropore + external area ^b (m ² g ⁻¹)	Micropore volume ^b (cm ³ g ⁻¹)	Total pore volume ^c (cm ³ g ⁻¹)	Mesoporous volume (cm ³ g ⁻¹)	BET pore size (nm)	Mean particle size (nm)
<i>n</i> -NiO/SiO ₂	91.50	93.18	5.17	88.01	0.0024	0.2301	0.2277	9.987	32.19
<i>n</i> -FeO/SiO ₂	97.31	99.11	7.02	92.08	0.0033	0.3712	0.3678	14.977	30.26
<i>n</i> -CoO/SiO ₂	48.96	50.06	7.25	42.80	0.0035	0.0957	0.0922	7.579	49.92

^a Represents the values calculated at a relative pressure (P/P_0) of N₂ equal to 0.301. ^b Represents the values calculated from *t*-plot method. ^c Represents the total pore volume evaluated from nitrogen uptake at a relative pressure (P/P_0) of N₂ equal to 0.98.

prevent metal particle agglomeration efficiently during high temperature calcination treatment. The BET surface area of *n*-NiO/SiO₂, *n*-FeO/SiO₂ and *n*-CoO/SiO₂ are 93.18 m² g⁻¹, 99.11 m² g⁻¹ and 50.06 m² g⁻¹, respectively. One can see that the BJH pore width distributions are in wide range from 0 nm to 160 nm, while the majority of the pores of all experimented catalysts are with a width less than 30 nm. Furthermore, the average BET pore width is calculated as 9.9 nm, 14.9 nm and 7.5 nm for *n*-NiO/SiO₂, *n*-FeO/SiO₂ and *n*-CoO/SiO₂, respectively. The pores with higher sizes (50 nm to 150 nm) occurred in the mesoporous and macroporous region may be because of the formation of voids due to inter-nanoparticles in contact.

The morphological appearance of the fresh *n*-NiO/SiO₂, *n*-FeO/SiO₂ and *n*-CoO/SiO₂ catalysts are exhibited in Fig. 4(a-c). Particle size distribution of respective nanoparticles are also exhibited. From the image, it is clearly visible that the particles are found uniformly distributed with various shapes covering a narrow range of sizes. However, crystallite in *n*-FeO/SiO₂ exhibit more or less circular disc morphology with almost similar particle size and dispersion, supporting the particle distribution histogram. While, *n*-NiO/SiO₂ and *n*-CoO/SiO₂ can be seen agglomerated to form giant particles in some area. This agglomeration results in structural intricacy leads to difficulties in reduction, supporting a higher temperature H₂-TPR curve (Fig. 6). ImageJ software was used to measure the actual particle sizes. The average particle sizes of all three compounds are lying in the range of 35–50 nm, supporting our BET and XRD report. EDX mapping report of each samples are shown in Fig. 5, assuring the presence of Ni, Fe, Co, Si and O elements.

The H₂-TPR profiles of *n*-NiO/SiO₂, *n*-FeO/SiO₂ and *n*-CoO/SiO₂ are shown in Fig. 6. The H₂-TPR profile of *n*-NiO/SiO₂ exhibit a single peak in between 300 °C and 692 °C can be assigned to the complete reduction of *n*-NiO species, supporting previous records.^{25,26} *n*-NiO/SiO₂ catalyst exhibits only one hydrogen conception peak in between 297 °C and 670 °C with a maximum at 420 °C. This individual peak indicates a homogeneous metal support interaction between nickel and silicate. It can be noted that *n*-NiO/SiO₂ could be reduced in between 300–600 °C supporting previous reports on Ni-based compounds.²⁷ H₂-TPR profile of *n*-NiO/SiO₂ starts from 297 °C and hence it can be assumed there is no silica free dispersed nickel oxide. However, Ermakova *et al.*¹⁵ reported that silica free nickel oxide reduces in between 236 °C and 246 °C. Furthermore, the H₂-TPR profile of *n*-NiO/SiO₂ quantifies a H₂ conception of 330.3 mL g_{cat}⁻¹. *n*-NiO/SiO₂ catalyst exhibits a broad reduction profile irrespective of the conventional metal supported catalysts.²⁸ However, it can be speculate that this strong nickel metal and silicate support interaction may results in difficulty in its reduction.²⁵ Furthermore, the existence of the reduction peak towards a higher value can be attributed to the presence of some higher sized *n*-NiO particles. Moreover, the denser SiO₂ support may cause difficulty in hydrogen diffusion and NiO reduction, supporting the presence of NiO peaks in the XRD results after reduction at 550 °C (Fig. 2(a)). H₂-TPR profile of *n*-FeO/SiO₂ exhibits one peak from 264 °C to 448 °C with a maximum value at 388 °C can be attributed to the reduction of Fe₂O₃.²⁹ Usually Fe has a lower tendency to form a strong

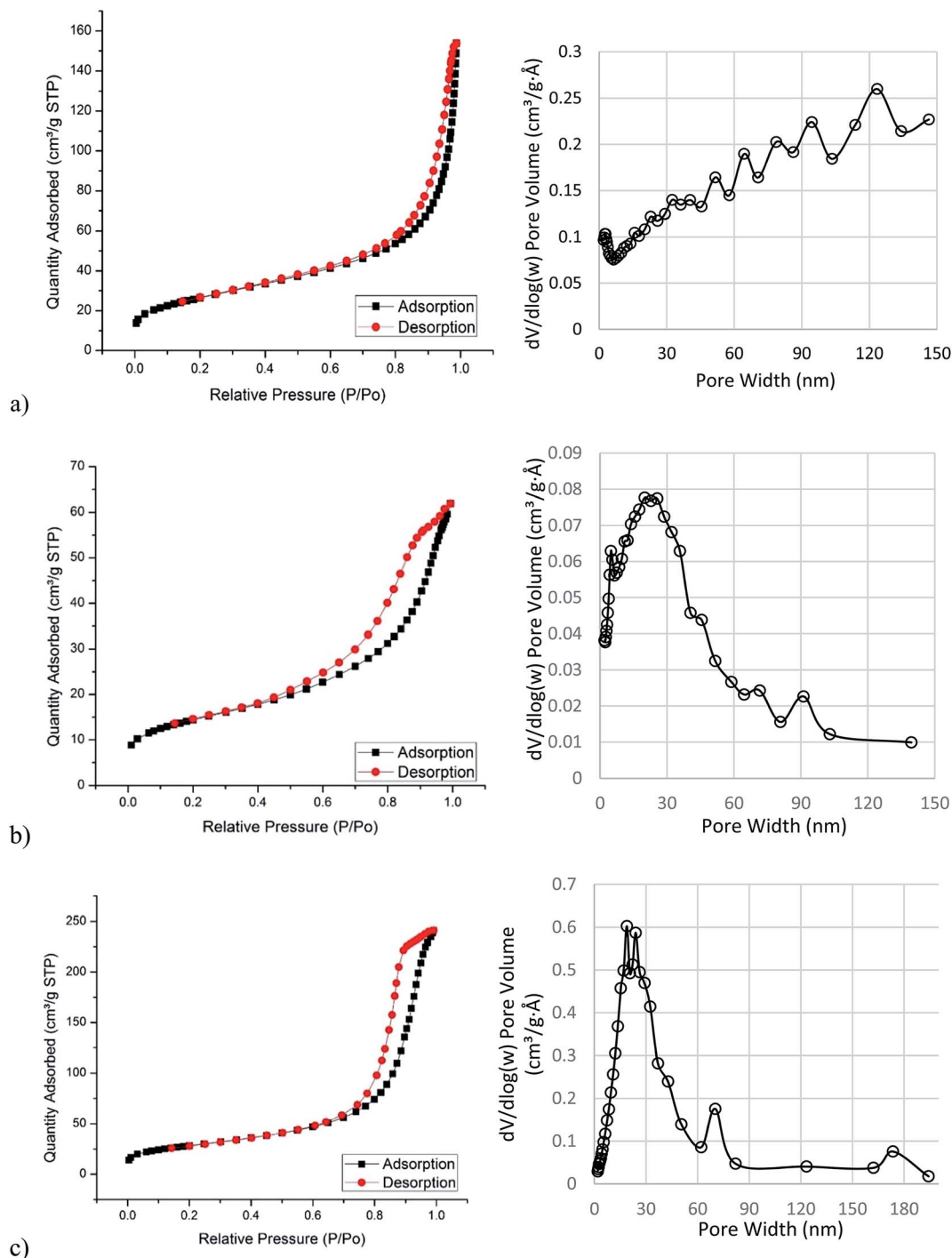


Fig. 3 N_2 -adsorption–desorption isotherms of the (a) n -NiO/SiO₂, (b) n -FeO/SiO₂ and (c) n -CoO/SiO₂ catalysts. The pore diameter distributions calculated with Barrett–Joyner–Halenda (BJH) method is shown near to each isotherm.

interaction with SiO₂.³⁰ However, formation of second peak indicates the noticeable shift of complete reduction of n -FeO/SiO₂ towards a higher temperature values. Reduction of n -CoO/SiO₂ accomplished in three stages. The peak in the temperature range from 243 °C to 360 °C can be accredited to double stage reduction of spinel as Co₃O₄ to CoO and to Co.³¹ While, n -Co/SiO₂ does not show any peaks above 600 °C reveals its weak metal support interaction compared to that in n -NiO/SiO₂.

Catalytic methane decomposition

Preliminary catalytic activity tests were conducted with all nanocatalysts in order to track the active temperature zone of each catalyst and results are exhibited in Fig. 7. Temperature programmed methane decomposition was conducted from 200 °C to 900 °C with a temperature ramp of 5 °C min⁻¹. Temperature programmed methane decomposition results reveal that

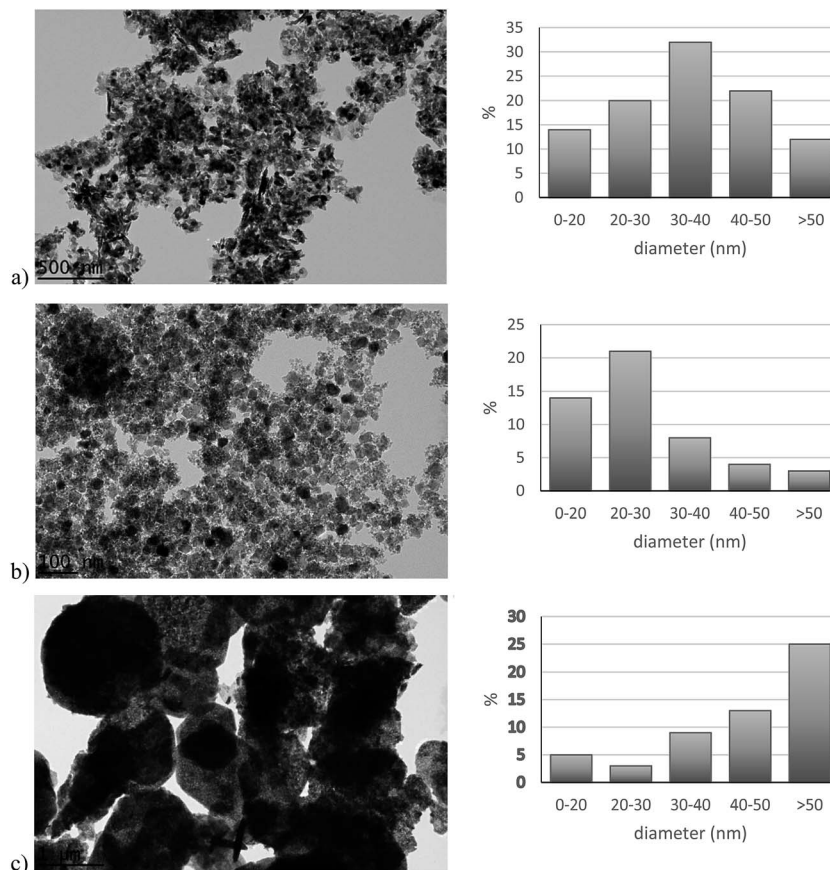


Fig. 4 TEM images and particle size distribution histogram of (a) *n*-NiO/SiO₂, (b) *n*-FeO/SiO₂ and (c) *n*-CoO/SiO₂. 50 nanoparticles were considered to plot particle size distribution histogram. ImageJ software was used to measure particle size.

n-Ni/SiO₂ catalyst is really active from 450 °C to ~730 °C with a maximum hydrogen production values of 57.28% at 730 °C and undergone fast deactivation upon increasing temperature. While, *n*-Co/SiO₂ exhibits an active zone from 510 °C to 645 °C. The maximum hydrogen production occurred over *n*-Co/SiO₂ is 22.3% at 645 °C. Furthermore, hydrogen production observed over *n*-Fe/SiO₂ was almost negligible when compared with that of Ni and Co based catalysts. *n*-Fe/SiO₂ produced 7.8% of hydrogen at its most active temperature and the active temperature range was very narrow. A gradual increase in hydrogen percentage was observed above 800 °C with all experimented catalysts can be attributed to the endothermic nature of methane decomposition reaction. Based on the results of temperature programmed methane decomposition, isothermal methane decomposition experiments were conducted for detailed catalysis evaluation at temperatures like 500 °C, 600 °C and 700 °C.

Fig. 8 shows the changes in hydrogen production percentage with time on stream for the TCD over *n*-Ni/SiO₂, *n*-Fe/SiO₂ and *n*-Co/SiO₂ catalysts at 500 °C, 600 °C and 700 °C. Influence of temperature on hydrogen production, activity and temperature sustainability of each catalyst are analyzed. All isothermal examinations were conducted with 99.995% methane. Rosemount Analytical X-STREAM detected only hydrogen and methane as gaseous products as indicated in the balanced

methane decomposition equation ($\text{CH}_4 \rightarrow 2\text{H}_2 + \text{C}$). The maximum hydrogen production percentage was observed in the very beginning of methane decomposition experiment, just after the contact of methane with catalyst. Afterwards, the hydrogen production found decreased gradually with time on stream according to the performance of catalyst. Fig. 8(a) shows that, *n*-Ni/SiO₂ catalyst exhibits a wide range of activity with hydrogen production from 17% to 65% in the experimented temperatures. The experiments were extended up to 240 minutes in order to evaluate the stability of *n*-Ni/SiO₂. Maximum hydrogen production were observed at 700 °C with *n*-Ni/SiO₂ catalyst, while catalyst was deactivated rapidly and turn out to be completely inactive within 100 minutes of experiment. This fast deactivation may be attributed to its thermal degradation at higher temperature.³ It is interesting to notice that, *n*-Ni/SiO₂ maintain its activity even after 240 minutes of experimental duration with a very low catalytic deactivation at 600 °C and 500 °C. However, minimum deactivation was observed at 500 °C. Furthermore, it is worth pointing out that the experimented *n*-Ni/SiO₂ catalyst is noticeably superior to the naked and supported Ni-based catalyst prepared by conventional methods at a temperature range of 500 °C–700 °C,^{32–36} clearly demonstrate the advantage of co-precipitation cum modified Stöber method for preparation of *n*-Ni/SiO₂ catalyst. Undesirably, *n*-Fe/SiO₂ catalyst was active at 700 °C only. Furthermore,

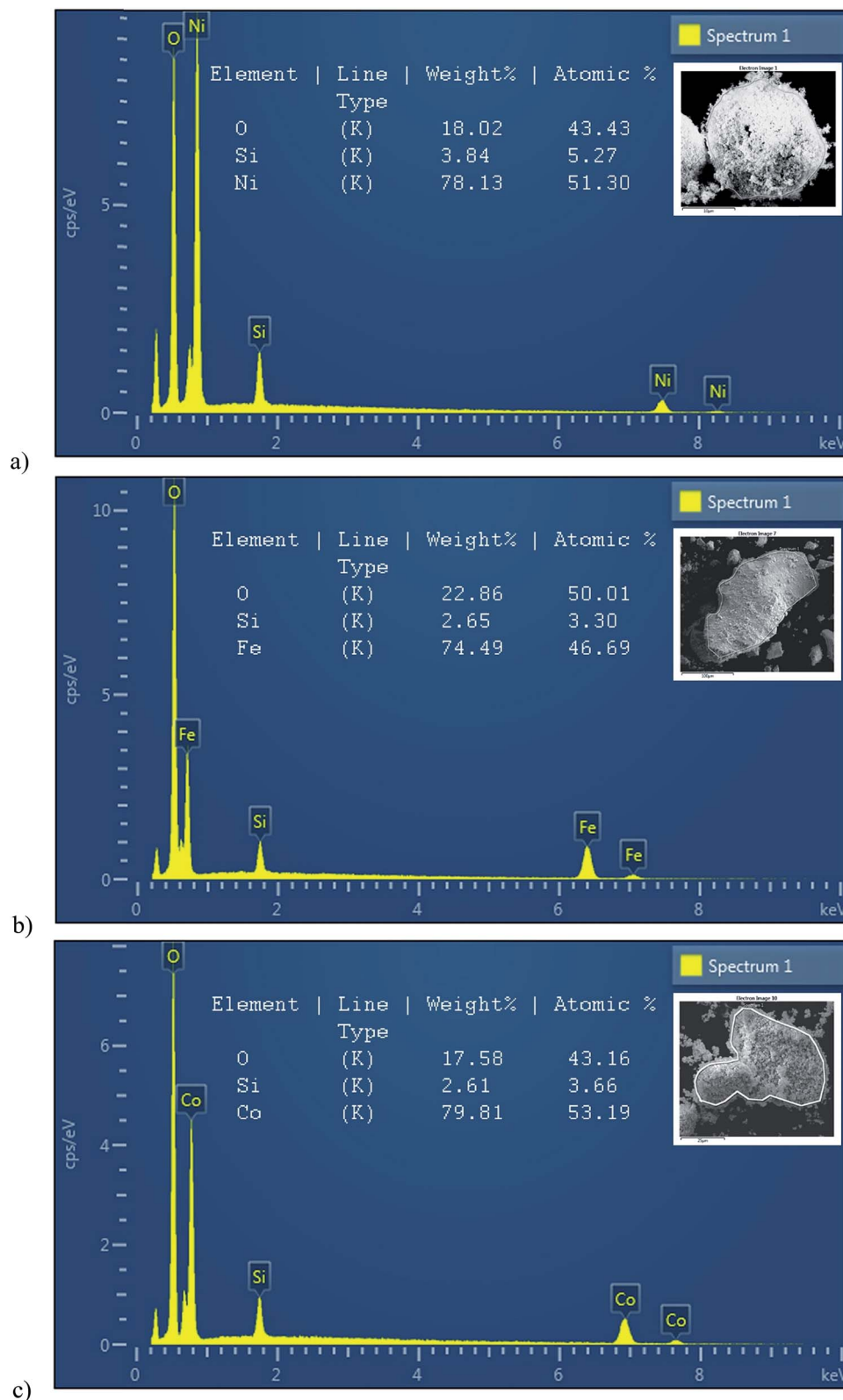


Fig. 5 EDX mapping and elemental composition of (a) *n*-NiO/SiO₂, (b) *n*-FeO/SiO₂ and (c) *n*-CoO/SiO₂.

the initial hydrogen production was very less (12.2%) compared to *n*-Ni/SiO₂ catalyst and reached negligible value by 1 hour of stream. It was completely inactive at experimented

temperatures like 600 °C and 500 °C as observed in temperature programmed methane decomposition (Fig. 7). *n*-Co/SiO₂ given moderate initial hydrogen production at 700 °C and 600 °C.

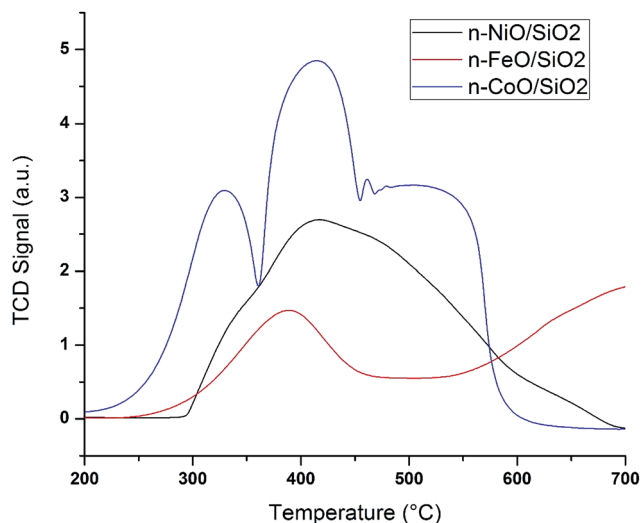


Fig. 6 H₂-TPR profile of *n*-NiO/SiO₂, *n*-FeO/SiO₂ and *n*-CoO/SiO₂.

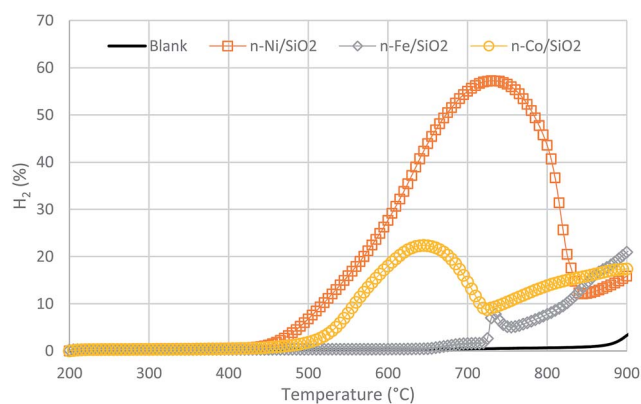


Fig. 7 Hydrogen production in percentage during temperature programmed methane decomposition over 1 g of *n*-Ni/SiO₂, *n*-Fe/SiO₂ and *n*-Co/SiO₂ catalysts. Temperature range 200–900 °C, flow rate 0.64 L min⁻¹.

While, catalytic stability was pitiable and dip to 5% within 10 minutes after methane stream reached the catalyst, similar rapid catalytic deactivation were observed by Lee *et al.*³⁷ over Co-based catalysts. It is reported that higher methane decomposition to hydrogen and nano-carbon occurs over coalesced metal particles, while it continues until the crystal size of sintered particle favor the nano-carbon growth.³⁸ It is worth to notice that the Ni-particle agglomeration is very less after methane decomposition as shown in TEM images (Fig. 11), results in higher hydrogen production (Fig. 8(a)) as well as huge carbon yield (Fig. 10). However, the lower activity of *n*-Co/SiO₂ (Fig. 8(c)) and *n*-Fe/SiO₂ (Fig. 8(b)) may be attributed to the sintering of metal particle to giant sizes which exceed the critical size for carbon nano-filament growth, as observed in Fig. 12 and 13, respectively. Furthermore, Ashok *et al.*³⁹ reported that metal particles of very large size were unable to grow carbon nano-filaments. Among the studied catalysts, *n*-Ni/SiO₂ catalyst is superior to Fe and Co based catalyst by all aspects. It is observed

that the initial catalytic activity and deactivation rate increases as increasing decomposition temperature, indicates the temperature sensitivity of TCD process. However, it is worth to note that the isothermal methane conversion over all experimented catalyst clearly follows the hydrogen production percentage and active temperature zone revealed by temperature programmed methane decomposition (Fig. 7). Hence, temperature programmed methane decomposition can be considered as an efficient step in order to identify catalytically active temperature zone of any catalyst.

Characterization of produced nanocarbon

Fig. 9 displays the XRD patterns of *n*-Ni/SiO₂, *n*-Fe/SiO₂ and *n*-Co/SiO₂ catalysts after TCD process at experimented temperatures. XRD peaks for *n*-Fe/SiO₂ after TCD at 500 °C and 600 °C were omitted as carbon production was negligible at those temperatures. Graphitic carbon produced over *n*-Ni/SiO₂ catalyst can be identified by the diffraction peaks at $2\theta = 26.26^\circ$ and 44.45° as indicated in Fig. 9(a). Those peaks are in good agreement with the JCPDS no. 98-005-3781 for graphite. However, reduced Ni-phases can be recognised at peaks $2\theta = 44.5^\circ$, 51.83° and 76.28° , confirmed with Ni peaks in JCPDS no. 01-070-1849. *n*-Fe/SiO₂ and *n*-Co/SiO₂ produced graphitic carbon as the peaks observed at $2\theta = 26.38^\circ$ and 44.39° in Fig. 9(b and c), are in good agreement with JCPDS no. 00-041-1487. Furthermore, the presence of iron carbide (Fe₃C) can be identified over *n*-Fe/SiO₂ catalyst after TCD (Fig. 9(b)) with the peaks at $2\theta = 37.76^\circ$, 45.01° , 70.88° and 78.65° , correspond to the peaks in JCPDS no. 00-034-0001. The intensity of peaks corresponds to graphite produced over *n*-Fe/SiO₂ and *n*-Co/SiO₂ are not high as those observed with *n*-Ni/SiO₂. However, it is observed that the graphitization intensity of produced nanocarbon improved as increasing decomposition temperature. It is clear from the amendment of the carbon peaks to a higher values in Fig. 9(a and c) in a similar manner to those produced over Ni impregnated zeolite catalyst as observed by Nasir Uddin *et al.*⁴⁰

Enormous quantity of carbon were formed over *n*-Ni/SiO₂ compared to *n*-Co/SiO₂ and *n*-Fe/SiO₂. The carbon yield percentage over each catalyst at respective temperatures were calculated with the following equation^{41,42} and the results are depicted in Fig. 10. The carbon yield of the catalysts was evaluated based on the extent of methane conversion against time on stream at a CH₄ flow rate of 0.64 L min⁻¹. Carbon deposition period was 5 hours for *n*-Ni/SiO₂ at 500 °C and 600 °C, while all other percentages are up to the complete deactivation of respective catalyst.

$$\text{Carbon yield (\%)} = \frac{\text{weight of deposited carbon on the catalyst}}{\text{weight of metal portion}} \times 100$$

Fig. 10 comprises the comparison of produced carbon yield over each experimented catalyst which reveals that *n*-Ni/SiO₂ produced very high quantity of nano-carbon compared to *n*-Co/SiO₂ and *n*-Fe/SiO₂. *n*-Ni/SiO₂ produced 4947.3% of carbon at

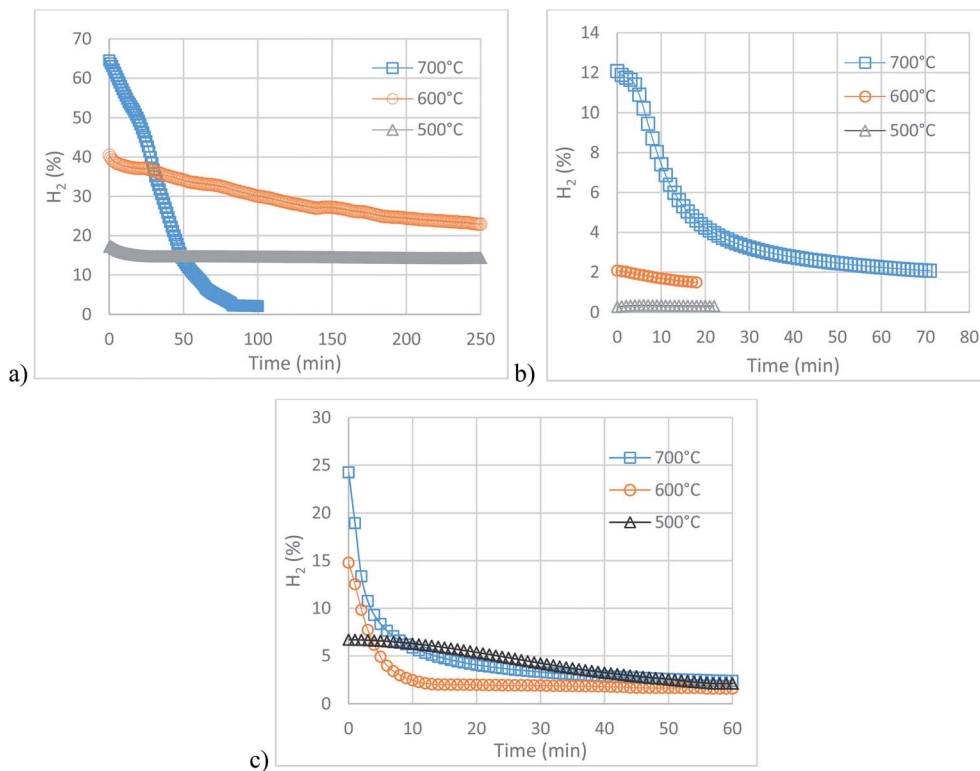


Fig. 8 Hydrogen formation percentage during isothermal methane decomposition over (a) *n*-Ni/SiO₂, (b) *n*-Fe/SiO₂ and (c) *n*-Co/SiO₂ catalysts at different temperature. Flow rate = 0.64 L min⁻¹ and catalyst weight = 0.5 g.

600 °C during 5 hours of experiment. Hence, it was not deactivated during the experimented period. While, it produced 1372.6% nano-carbon at 700 °C before it deactivated in 100 minutes. However, 105.2% and 144.6% nano-carbon were formed over *n*-Co/SiO₂ catalyst before its complete deactivation at 700 °C and 600 °C, respectively. Whereas, it was very low at 600 °C as *n*-Co/SiO₂ undergone fast deactivation. Very regrettable performance was shown by *n*-Fe/SiO₂, which produced 104.4% of nano-carbon at 700 °C. Though, *n*-Fe/SiO₂ was almost inactive at 500 °C and 600 °C as observed in temperature programmed methane decomposition (Fig. 7). The observed carbon yield is outstanding compared to many other available results over Ni-based catalyst.⁴¹ However, the performance of *n*-Co/SiO₂ and *n*-Fe/SiO₂ are pitiable. Likewise, such disgraceful results were reported by Zadeh and Smith⁴³ over Co-based catalysts. This deprived catalyst performance can be attributed to the faster particle agglomerations and complete catalyst encapsulation with produced carbon as shown in TEM images (Fig. 12 and 13).

Fig. 11(a–c) displays TEM images of produced nano-carbon over *n*-Ni/SiO₂ catalyst at 700 °C, 600 °C and 500 °C, respectively. However, TEM images of produced nano-carbon over *n*-Co/SiO₂ and *n*-Fe/SiO₂ exhibited in Fig. 12 and 13, respectively.

TEM images (Fig. 11 and 12) elucidate that *n*-Ni/SiO₂ and *n*-Co/SiO₂ mainly produce carbon nano-tubes, while small quantity of nano-fibers were also identified. Hence, nano-tube can be recognized with the presence of a hollow cavity, though it is absent with nano-fibers.⁴⁴ Ni and Co metals can be seen at the

dip of formed nano-carbon. Very low carbon yield observed over *n*-Co/SiO₂ at 600 °C can be attributed to the complete encapsulation of catalyst with produced nano-carbon and heavy agglomeration of catalyst as shown in Fig. 12(b). However, pear or diamond shaped metals with its sharp tail inserted to the produced nano-tubes can be seen in Fig. 11(a–c) and in Fig. 12(c), following tip-growth carbon formation mechanism,⁴⁵ which is reinforcing many previous works.^{46–48} Furthermore, *n*-Ni/SiO₂ catalyst also produces different types of nano-carbons as follows: fish-bone nanocarbon, carbon nano tubes with open end, carbon nano tubes with closed end and carbon nanotube with Ni particle embedded in it. Such varieties of nano-carbons were absent with *n*-Fe/SiO₂. In addition to carbon nano-tubes, irregular carbon formulation was observed over *n*-Co/SiO₂ and *n*-Fe/SiO₂, could be attributed to the occurrence metal particle fragmentation which maintains the availability of more active metal phases.⁴⁹ The availability of such higher active metal phases because of the diffusion of supersaturated nano-carbon results in the formation of more nano-carbon around the catalyst particles by methane decomposition which leads to its complete encapsulation. Furthermore, the carbon diffusion occurred may be attributed to the less effective interaction between Co and Fe metals with the silicate supports or their incomplete shielding which results in the domination of Co and Fe metal phases at their surface. It is obvious from the displayed TEM images (Fig. 12 and 13) that *n*-Co/SiO₂ and *n*-Fe/SiO₂ catalysts were rapidly agglomerated and encapsulated with produced carbon after methane came in contact with it and

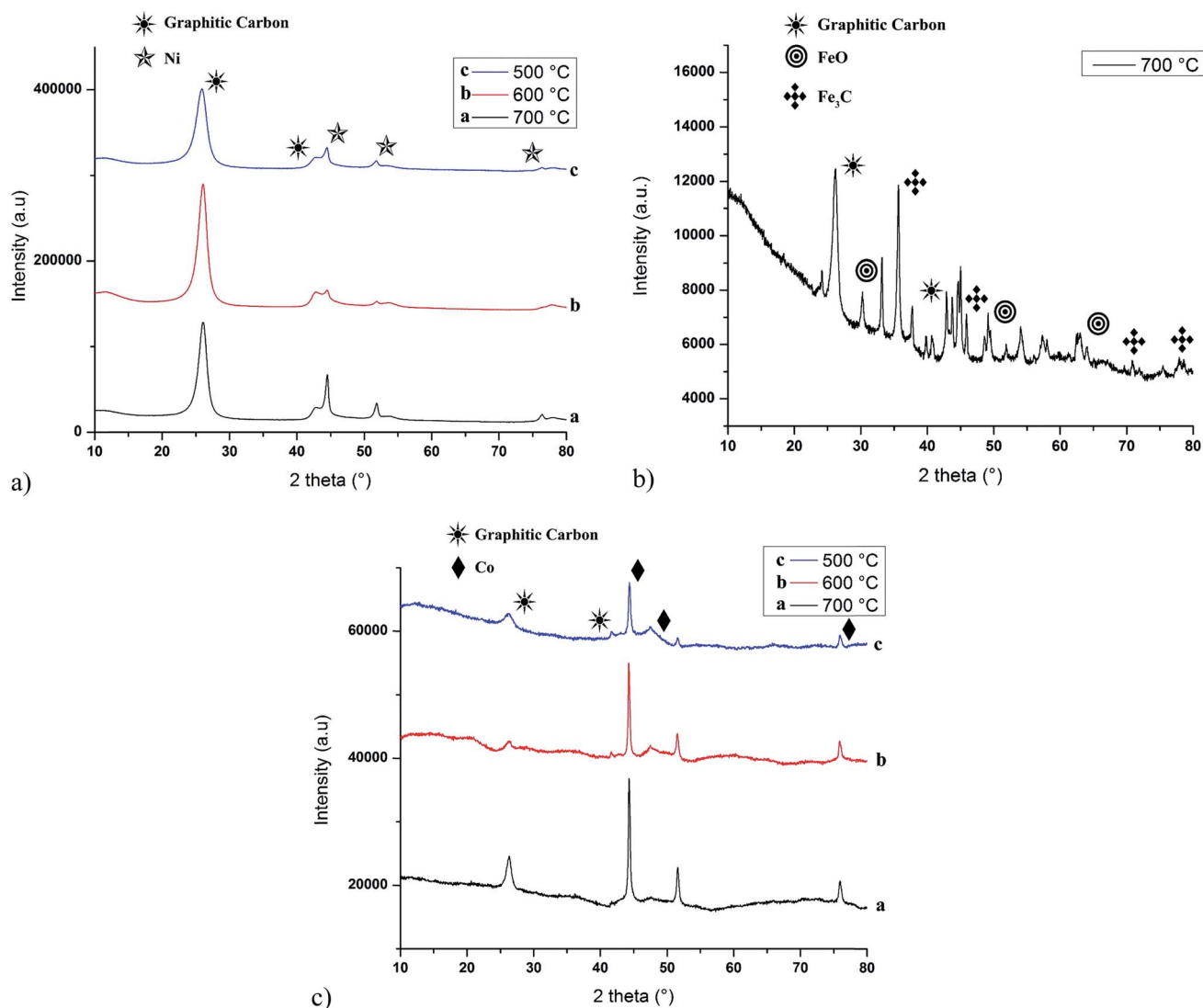


Fig. 9 XRD patterns of (a) *n*-Ni/SiO₂ (b) *n*-Fe/SiO₂ and (c) *n*-Co/SiO₂ after isothermal methane decomposition at different temperature. Peaks corresponds to graphitic carbon, Ni, FeO, Fe₃C and Co are indicated.

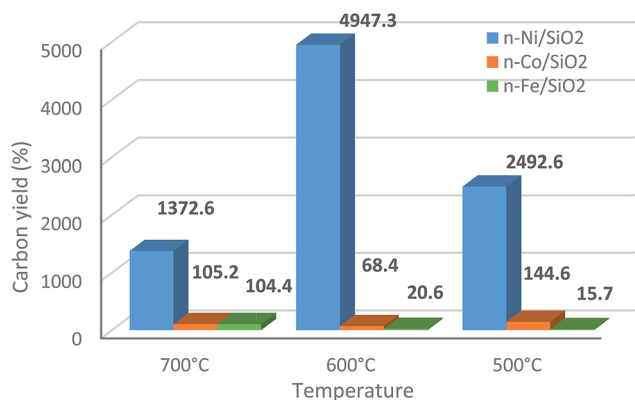


Fig. 10 Comparison of calculated carbon yield in percentage produced over respective catalyst at 700 °C, 600 °C and 500 °C.

hence loose its activity completely. However, such metal particle fragmentation is absent with *n*-Ni/SiO₂ because of the efficient interaction between Ni metal phase and silicate supports results in the enhanced activity and stability. It is worth to note that nano-carbon with larger diameter were formed over *n*-Co/SiO₂ at 600 °C and over *n*-Fe/SiO₂ at 700 °C may be attributed to the formation of carbon over agglomerated larger catalysts particles, and hence encapsulated by carbon leads to their faster deactivation. Similar result was already reported by Jana *et al.*³¹ over the spinel catalysts. It was reported that the outer diameter of the carbon nanotubes greatly depend on the size of catalyst particles. Hence, larger particles produce carbon nanotubes with larger diameter.⁵⁰ Furthermore, Ermakova *et al.*¹⁵ reported such a speedy catalyst encapsulation with carbon over Fe-based catalyst. However, there is no such agglomeration or encapsulation can be seen with *n*-Ni/SiO₂ (Fig. 11) which endure a longer activity and produces a huge carbon deposition at all their experimented temperatures. The formation of nano-carbon over

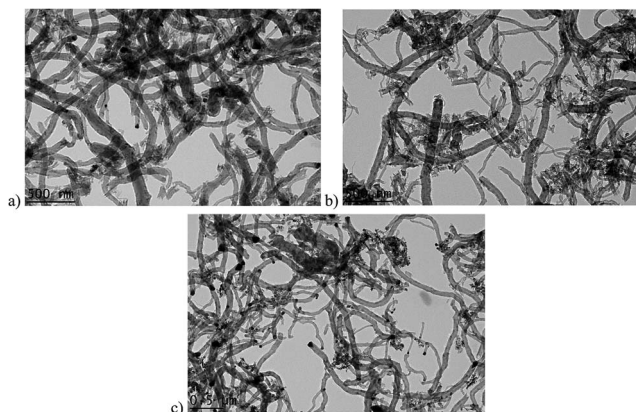


Fig. 11 TEM images of produced nano-carbon over *n*-Ni/SiO₂ at (a) 700 °C, (b) 600 °C and (c) 500 °C.

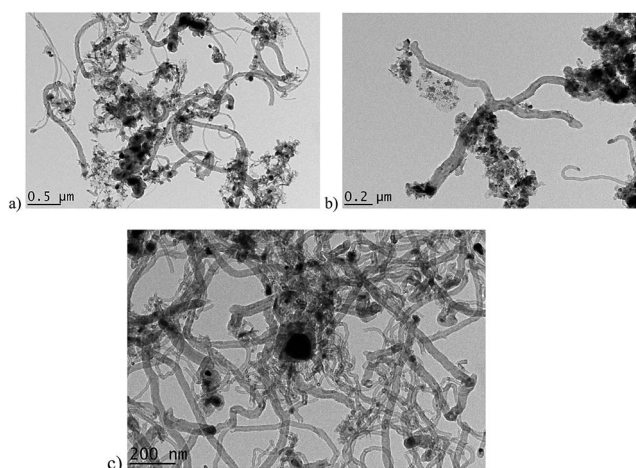


Fig. 12 TEM images of produced nano-carbon over *n*-Co/SiO₂ at (a) 700 °C, (b) 600 °C and (c) 500 °C.

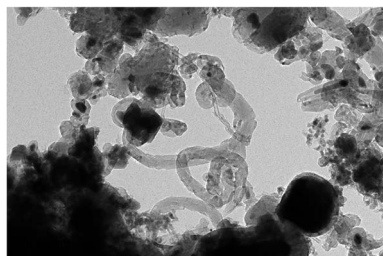


Fig. 13 TEM images of produced nano-carbon over *n*-Fe/SiO₂ at 700 °C.

n-Ni/SiO₂ occurred at the interface between the Ni particle and silicate support and hence metal is detached from support.⁵¹ However, Ni-particle maintained its activity at the surface of growing carbon filaments which results in the longer activity of *n*-Ni/SiO₂. Furthermore, almost similar graphite formation was observed with *n*-Co/SiO₂, while the carbon deposited on it encapsulate active metal face and hence results in its rapid deactivation.⁵² In accordance to previous reports,⁵³ our results also reveals that stable catalytic performance and catalytic

decomposition depend on the catalysts, catalytic characteristics and operating parameters.

FESEM images of produced nano-carbon over *n*-Ni/SiO₂ at respective temperature are displayed in Fig. 14(a–c) and the diameter distribution histogram in Fig. 14(d). FESEM images disclose that the produced nano-carbons have smooth elliptical shape with diameter covering a range of 5 nm to 145 nm. It is very difficult to compute the actual length of the carbon nano-carbon as they exist in an interweaving manner. However, it can speculate that the length exceeds some micrometers. The brighter spot observed in Fig. 14(a–c) at the tips of carbon nanotubes are Ni-metal particle and it is worth to note that the diameter of nano-carbon are similar to that of Ni-particles. The diameter of nano-carbons were measured with ImageJ software. The average diameter calculated from 50 nano-carbons were 35.75 ± 7.8 nm, 52.64 ± 11.5 nm and 56.34 ± 15.2 nm at 700 °C, 600 °C and 500 °C, respectively. These results are in well consistent with the Ni-crystallite size calculated from XRD patterns using Scherrer equation. Hence, calculated crystallite sizes are 34.2 nm, 47.03 nm and 50.22 nm at 700 °C, 600 °C and 500 °C, respectively. This strong consistency between carbon diameter and Ni-crystallite size are clearly reveals the dependability between them, supporting previous reports.^{54,55} Furthermore, diameter distribution histogram (Fig. 14(d)) reveals that the diameters of the most of produced nano-carbons are in between 40 nm and 80 nm. It is clear from the FESEM images that the morphology and quality of produced nano-carbons are almost similar at all experimented temperature over *n*-Ni/SiO₂ catalyst. However, methane decomposition at 700 °C produced more nano-carbon with very low (<40 nm) diameter compared to 600 °C and 500 °C. Furthermore, nano-carbon with open end, closed end and with metal particle at the dip also can clearly found in the FESEM images, seconding the TEM images shown in Fig. 11.

Conclusion

Thermocatalytic decomposition of methane conducted over *n*-Ni/SiO₂, *n*-Fe/SiO₂ and *n*-Co/SiO₂ catalysts to produce hydrogen and nano-carbon. Active metallic phases of catalysts were prepared by co-precipitation method from corresponding metal nitrates. Modified Stöber method was adopted to develop a safeguard support for active nano-metal with silicate using TEOS and C18TMS as silicate precursors. During methane decomposition catalytic activity examination, *n*-Ni/SiO₂ catalyst exhibited an outstanding performance compared to *n*-Fe/SiO₂ and *n*-Co/SiO₂ catalysts. The poor performance of *n*-Fe/SiO₂ and *n*-Co/SiO₂ catalysts were attributed to the formation of giant metal particles with unfavorable crystal size for growth of nano-carbon. Furthermore, formation of irregular shaped nano-carbons over Fe and Co-based catalyst because of the metal particle fragmentation also retarding their activity. While, such defects were absent with *n*-Ni/SiO₂ catalyst, which produce fine carbon nano-tubes with active metal at the tip. Maximum hydrogen production over *n*-Ni/SiO₂ was 64.4% at 700 °C, while minimum deactivation after 240 minutes of examination was found at 500 °C. A variety of nano-carbons were formed over *n*-

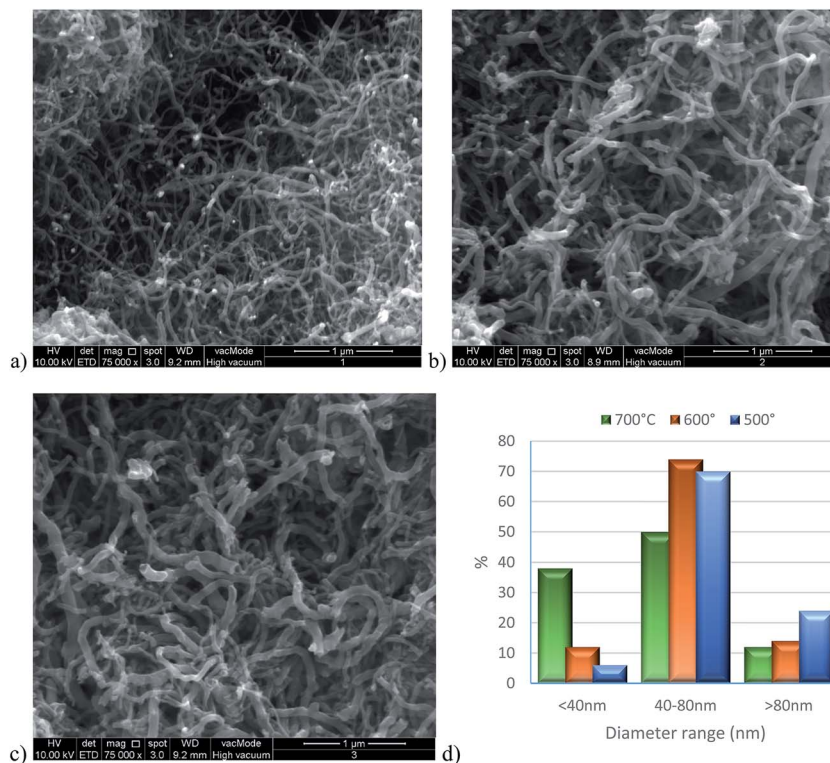


Fig. 14 FESEM images of produced nano-carbon over n -Ni/SiO₂ catalyst at (a) 700 °C, (b) 600 °C and (c) 500 °C. (d) Nano-carbon diameter distribution histogram. Diameter of 50 nano-carbons were measured with ImageJ software.

Ni/SiO₂ catalyst. According to our experimental results, the performance of analyzed catalysts in terms of its stability and activity follow this order n -Ni/SiO₂ > n -Co/SiO₂ > n -Fe/SiO₂. Considering the abundance and cheap rate of nickel precursors as well as considerably simple and room temperature catalyst production method, the nano-structured n -Ni/SiO₂ prepared by co-precipitation cum modified Stöber method is a kind of promising material for the production of GHG free H₂ through the catalytic decomposition of methane.

Acknowledgements

The authors gratefully acknowledge financial support from the postgraduate Research Fund (UM.C/HIR/MOHE/ENG/11), University of Malaya, Malaysia. Authors would like to extent thanks to both reviewers for their constructive comments and suggestions. Help from Mr Zaharudin bin Md. Salleh, Science Officer Assistant, Department of Geology, University of Malaya for XRD analysis is also sincerely acknowledged.

References

- R. Ghosh Chaudhuri and S. Paria, *Chem. Rev.*, 2012, **112**, 2373–2433.
- Y. Zhu, C. N. Lee, R. A. Kemp, N. S. Hosmane and J. A. Maguire, *Chem.-Asian J.*, 2008, **3**, 650–662.
- U. P. M. Ashik and W. M. A. W. Daud, *RSC Adv.*, 2015, **5**, 46735–46748.
- A. F. Cunha, J. J. M. Órfão and J. L. Figueiredo, *Int. J. Hydrogen Energy*, 2009, **34**, 4763–4772.
- A. Venugopal, S. Naveen Kumar, J. Ashok, D. Hari Prasad, V. Durga Kumari, K. B. S. Prasad and M. Subrahmanyam, *Int. J. Hydrogen Energy*, 2007, **32**, 1782–1788.
- U. P. M. Ashik, W. M. A. Wan Daud and H. F. Abbas, *Renewable Sustainable Energy Rev.*, 2015, **44**, 221–256.
- A. E. Awadallah, A. A. Aboul-Enein and A. K. Aboul-Gheit, *Energy Convers. Manage.*, 2014, **77**, 143–151.
- B. Dou, C. Wang, Y. Song, H. Chen and Y. Xu, *Energy Convers. Manage.*, 2014, **78**, 253–259.
- S. Takenaka, S. Kobayashi, H. Ogihara and K. Otsuka, *J. Catal.*, 2003, **217**, 79–87.
- S. Takenaka, H. Ogihara, I. Yamanaka and K. Otsuka, *Appl. Catal.*, A, 2001, **217**, 101–110.
- S. Takenaka, M. Serizawa and K. Otsuka, *J. Catal.*, 2004, **222**, 520–531.
- S. Karnjanakom, G. Guan, B. Asep, X. Du, X. Hao, C. Samart and A. Abudula, *Energy Convers. Manage.*, 2015, **98**, 359–368.
- S. R. Yahyavi, M. Haghighi, S. Shafiei, M. Abdollahifar and F. Rahmani, *Energy Convers. Manage.*, 2015, **97**, 273–281.
- M. A. Ermakova, D. Y. Ermakov, A. L. Chuvilin and G. G. Kuvshinov, *J. Catal.*, 2001, **201**, 183–197.
- M. A. Ermakova and D. Y. Ermakov, *Catal. Today*, 2002, **77**, 225–235.
- L. Guzzi, R. A. van Santen and K. V. Sarma, *Catal. Rev.*, 1996, **38**, 249–296.

- 17 L. B. Avdeeva, D. I. Kochubey and S. K. Shaikhutdinov, *Appl. Catal., A*, 1999, **177**, 43–51.
- 18 A.-C. Dupuis, *Prog. Mater. Sci.*, 2005, **50**, 929–961.
- 19 Y. Li, S. Liu, L. Yao, W. Ji and C.-T. Au, *Catal. Commun.*, 2010, **11**, 368–372.
- 20 A. A. Al-Hassani, H. F. Abbas and W. M. A. Wan Daud, *Int. J. Hydrogen Energy*, 2014, **39**, 7004–7014.
- 21 M. Stjerndahl, M. Andersson, H. E. Hall, D. M. Pajeroski, M. W. Meisel and R. S. Duran, *Langmuir*, 2008, **24**, 3532–3536.
- 22 J. Zou, Y.-G. Peng and Y.-Y. Tang, *RSC Adv.*, 2014, **4**, 9693–9700.
- 23 W. Stöber, A. Fink and E. Bohn, *J. Colloid Interface Sci.*, 1968, **26**, 62–69.
- 24 Y. Li, J. Chen, L. Chang and Y. Qin, *J. Catal.*, 1998, **178**, 76–83.
- 25 L. Li, S. He, Y. Song, J. Zhao, W. Ji and C.-T. Au, *J. Catal.*, 2012, **288**, 54–64.
- 26 L. Li, P. Lu, Y. Yao and W. Ji, *Catal. Commun.*, 2012, **26**, 72–77.
- 27 X.-K. Li, W.-J. Ji, J. Zhao, S.-J. Wang and C.-T. Au, *J. Catal.*, 2005, **236**, 181–189.
- 28 R. Xie, D. Li, B. Hou, J. Wang, L. Jia and Y. Sun, *Catal. Commun.*, 2011, **12**, 380–383.
- 29 H. Jung and W. J. Thomson, *J. Catal.*, 1991, **128**, 218–230.
- 30 C. R. F. Lund and J. A. Dumesic, *J. Catal.*, 1981, **72**, 21–30.
- 31 P. Jana, V. A. de la Peña O'Shea, J. M. Coronado and D. P. Serrano, *Int. J. Hydrogen Energy*, 2012, **37**, 7034–7041.
- 32 W. Wang, H. Wang, Y. Yang and S. Jiang, *Int. J. Hydrogen Energy*, 2012, **37**, 9058–9066.
- 33 B. Zapata, M. A. Valenzuela, J. Palacios and E. Torres-Garcia, *Int. J. Hydrogen Energy*, 2010, **35**, 12091–12097.
- 34 G. D. B. Nuernberg, E. L. Foletto, C. E. M. Campos, H. V. Fajardo, N. L. V. Carreño and L. F. D. Probst, *J. Power Sources*, 2012, **208**, 409–414.
- 35 J. L. Figueiredo, J. J. M. Órfão and A. F. Cunha, *Int. J. Hydrogen Energy*, 2010, **35**, 9795–9800.
- 36 H. Puliylalil, U. Cvelbar, G. Filipic, A. D. Petric, R. Zaplotnik, N. Recek, M. Mozetic and S. Thomas, *RSC Adv.*, 2015, **5**, 37853–37858.
- 37 K.-Y. Lee, W.-M. Yeoh, S.-P. Chai, S. Ichikawa and A. R. Mohamed, *Fullerenes, Nanotubes, Carbon Nanostruct.*, 2012, **21**, 158–170.
- 38 L. B. Avdeeva, O. V. Goncharova, D. I. Kochubey, V. I. Zaikovskii, L. M. Plyasova, B. N. Novgorodov and S. K. Shaikhutdinov, *Appl. Catal., A*, 1996, **141**, 117–129.
- 39 J. Ashok, P. S. Reddy, G. Raju, M. Subrahmanyam and A. Venugopal, *Energy Fuels*, 2009, **23**, 5–13.
- 40 M. Nasir Uddin, W. M. A. Wan Daud and H. F. Abbas, *Energy Convers. Manage.*, 2015, **90**, 218–229.
- 41 S. K. Saraswat and K. K. Pant, *Int. J. Hydrogen Energy*, 2011, **36**, 13352–13360.
- 42 S.-P. Chai, C.-M. Seah and A. R. Mohamed, *J. Nat. Gas Chem.*, 2011, **20**, 84–89.
- 43 J. S. M. Zadeh and K. J. Smith, *J. Catal.*, 1998, **176**, 115–124.
- 44 P. Serp, M. Corrias and P. Kalck, *Appl. Catal., A*, 2003, **253**, 337–358.
- 45 A. K. Sinha, D. W. Hwang and L.-P. Hwang, *Chem. Phys. Lett.*, 2000, **332**, 455–460.
- 46 T. Baird, J. R. Fryer and B. Grant, *Carbon*, 1974, **12**, 591–602.
- 47 R. T. K. Baker, M. A. Barber, P. S. Harris, F. S. Feates and R. J. Waite, *J. Catal.*, 1972, **26**, 51–62.
- 48 P. A. Tesner, E. Y. Robinovich, I. S. Rafalkes and E. F. Arefieva, *Carbon*, 1970, **8**, 435–442.
- 49 C. H. Bartholomew, *Appl. Catal., A*, 2001, **212**, 17–60.
- 50 J. C. Guevara, J. A. Wang, L. F. Chen, M. A. Valenzuela, P. Salas, A. García-Ruiz, J. A. Toledo, M. A. Cortes-Jácome, C. Angeles-Chavez and O. Novaro, *Int. J. Hydrogen Energy*, 2010, **35**, 3509–3521.
- 51 Y. Zhang and K. Smith, *Catal. Lett.*, 2004, **95**, 7–12.
- 52 G. G. Kuvshinov, Y. I. Mogilnykh and D. G. Kuvshinov, *Catal. Today*, 1998, **42**, 357–360.
- 53 Y. Zhang and K. J. Smith, *Catal. Today*, 2002, **77**, 257–268.
- 54 A. de Lucas, A. Garrido, P. Sánchez, A. Romero and J. L. Valverde, *Ind. Eng. Chem. Res.*, 2005, **44**, 8225–8236.
- 55 V. R. Choudhary, S. Banerjee and A. M. Rajput, *J. Catal.*, 2001, **198**, 136–141.